

3D Spectroscopic Study of the Line Emitting Regions of Mrk 493

L. Č. Popović^{1,2}, A. A. Smirnova³, J. Kovačević^{1,2}, A.V Moiseev³, and V.L. Afanasiev³

Received _____; accepted _____

¹Astronomical Observatory, Volgina 7, 11160 Belgrade, Serbia

²Isaac Newton Institute, Yugoslavia Branch

³Special Astrophysical Observatory, Nizhnii Arkhyz, Karachaevo-Cherkesia, 369167 Russia

ABSTRACT

We report the results of 3D spectroscopic observations of Mrk 493 (NLS1 galaxy) with the integral-field spectrograph MPFS of the SAO RAS 6-m telescope. The difference in the slope of the optical continuum emission intensity across the nucleus part and an extensive continuum emission region is detected. The emission in lines ($H\alpha$, $H\beta$, [OIII], etc.) coincides with a composite nuclear region: an AGN plus a circum-nuclear star-forming ring observed in the HST UV/optical images. The [SII] emission region tends to be up to 1kpc around the center. The $H\alpha$ and $H\beta$ could be decomposed into three components (broad ~ 2000 km/s, intermediate ~ 700 km/s and narrow ~ 250 km/s). We found that width (~ 750 km/s) of the Fe II lines correspond to the intermediate component, that may indicate a non-BLR origin of the Fe II lines, or that a large fraction of the Fe II emission arise in the outer parts of the BLR. The weak broad component detected in the $H\alpha$, $H\beta$ and $He\lambda 4686$ may come from the unresolved central BLR, but also partly produced by violent starburst in the circum-nuclear ring. Moreover, diagnostic diagrams clearly show presence of the HII regions (not a Sy 1 nucleus) in the NLR of Mrk 493.

Subject headings: galaxies: active – galaxies: individual (Mrk 493) – galaxies: Seyfert

1. Introduction

Mrk 493, a narrow-line Seyfert 1 galaxy (NLS1), is known as an Active Galactic Nucleus with a strong Fe II emission (Osterbrock and Pogge 1985, Crenshaw et al. 1991). NLS1s have been recognized as a distinct type of Seyfert nuclei. The optical emission-line properties of NLS1s can be summarized as (e.g., Osterbrock & Pogge 1985, Komossa 2008): (i) The Balmer lines are only slightly broader than the forbidden lines such as the [O III] $\lambda 5007$ (typically less than 2000 km s^{-1}). (ii) The [O III] $\lambda 5007/H\beta$ intensity ratio is smaller than 3. (iii) They present the strong Fe II emission which are often seen in Sy 1s but generally not in Sy 2's. Moreover, the X-ray spectra of NLS1's are very steep (e.g. Boller et al. 1996, Leighly 1999ab) and highly variable (Boller et al. 1996; Leighly 1999a; Gliozzi et al. 2007). Also, it was found that NLS1s have less massive black hole masses than Sy 1s (Mathur 2000, Wang & Zhang 2007) and could be young Sy 1s (Botte et al. 2004). Even though NLS1s have been known for almost more than 20 years, it is still not clearly understood what NLS1s are in the context of the current AGN unified model (Nagao et al. 2001).

One of the interesting observational facts connected with NLS1 is that in their spectra a strong Fe II emission is present. It was shown by Boroson & Green (1992) that a strong anti-correlation between the strengths of the [OIII] and Fe II line intensities exists in the optical spectra, where NLS1s are showing the strongest Fe II and weakest [OIII] emission. The observed line widths and absence of the forbidden emission suggests that the Fe II lines are formed in the dense broad-line region (BLR), but photo-ionization models cannot account for all of the Fe II emission. The 'Fe II discrepancy' remains unsolved, though models which consider non-radiative heating with an overabundance of iron are promising (Joly 1993, Collin & Joly 2000). Also Mathur (2000) proposed that the strong Fe II emission observed in NLS1s may be connected with their large accretion rates and that a

collisional ionization origin of Fe II is possible.

Here we report 3D spectroscopic observations of Mrk 493. The aims of the observations were (i) to investigate the characteristics of the Fe II emitting region and possible their connection with other emitting regions ($H\alpha$, $H\beta$, [OIII], ...) and (ii) to map the circum-nuclear emitting gas in this type of AGN. In this paper we accepted a distance to Mrk 493 of 125.2 Mpc (for $H_0 = 75 \text{ km s}^{-1} \text{ Mpc}^{-1}$), where $1''$ on the sky corresponds to 610 pc at the galaxy distance.

2. Observations and data reduction

The observational data were obtained at the prime focus of the Russian 6-m telescope of the Special Astrophysical Observatory (SAO). The central region of the galaxy was observed with the MultiPupil Fiber Spectrograph (MPFS). MPFS (Afanasiev et al. 2001) takes simultaneous spectra from 256 spatial elements (constructed in the shape of square lenses) that form on the sky an array of 16×16 elements with the angular size 1 arcsec/element. Bundle of 17 fibers placed on the distance about 3.5 arcmin from the lens array provides the night-sky background spectra simultaneously with object's exposition. We have observed Mrk 493 twice in years 2004 and 2007, in the low- and high- resolution spectral modes (see Tab. 1).

The spectral ranges included numerous emission lines of ionized gas ([OI] λ 6300, [OIII] $\lambda\lambda$ 4959, 5007, [NII] $\lambda\lambda$ 6548, 6583, [SII] $\lambda\lambda$ 6717, 6731, the Balmer $H\alpha$ and $H\beta$ lines). The spectra were reduced using the IDL-based software developed at the SAO RAS, and the data reduction sequence is briefly described in Moiseev et al. (2004). Namely, the primary reduction included bias subtraction, flat-fielding, cosmic-ray hits removal, extraction of individual spectra from the CCD frames, and their wavelength calibration using a spectrum

of a He-Ne-Ar lamp. Subsequently, we subtracted the night-sky spectrum from the galaxy spectra. We corrected the effect of differential atmospheric refraction (offset shifting of galactic images at different wavelengths) by using the algorithm similar to described by Arribas et al. (1999). The data reduction result in a data cube in which a spectrum corresponds to each image ‘spaxel’¹ in two-dimensional field 16×16 arcsec. The seeing values shown in Table. 1 were estimated from the MPFS observations of stars right before the object observations. Here we fitted by 2D Moffat function the stars images in their data cubes.

Additionally we observed broad-band direct images of the galaxy in the filters B,V and R_C with the focal reducer SCORPIO (Afanasiev & Moiseev 2005). The seeing was 1.3 arcsec, the total expositions were 400 sec in B and 360 sec in V and R_C bands, respectively. These images seem slightly deeper than POSS and SDSS archival data, we confidently detected outer low-brightness grand-design structure in this barred galaxy (Fig. 1).

3. Results and discussion

3.1. The continuum and line fluxes distribution across Mrk 493 nucleus

First, we explore the brightness distribution across Mrk 493 nucleus in different wavelength bands. In Fig 2 we presented the maps of emission lines. Each pixel on these maps corresponds to the flux obtained by Gaussian fitting of the lines or simple by integration around 6200 \AA in the continuum. The maps of the [OIII] $\lambda\lambda 5007$ and [SII] $\lambda\lambda 6717, 6731$ were constructed using a single-Gaussian fitting, while the maps in the $H\beta$ and $H\alpha$ regions are separately constructed for the narrow as well as for the broad Gaussian components of these lines. Also, we made a map of the Fe II features (left and

¹ the spatial element of a 3D spectra

right from $H\beta$ + $[OIII]$ lines), integrating the all emission (after subtracting the continuum) in the wavelength range from 4500 – 4800 Å (blue shelf) and 5200 – 5500 Å (red shelf). The maximum of the Fe II emission corresponds to the optical center of Mrk 493 (i.e. the continuum emission).

In order to investigate the spatial extension of the emission-line regions we fitted the images of the star-like nucleus with 2D Moffat function. We assumed that the FWHM of the 2D Moffat function represents the dimension of the regions. The results of the fitting are shown in Fig. 2. We should note here that the sizes (FWHM) of the nuclear emission line region (except $[SII]$ lines) are almost the same or slightly larger ($2''$) than was the seeing during the observations ($1.7 \pm 0.2''$). Therefore, the dimension of the Fe II, $[OIII]$ and the narrow and broad Balmer line emitting regions seem to be practically the same. It might be caused by spatial resolution of the instrument, but in any case there is a compact $[OIII]$ region, smaller than continuum and $[SII]$ one (see Fig. 2). The $[SII]$ emission region tends to be up to 1 kpc around the center.

Also, we found that the continuum slope and the $H\alpha/H\beta$ line flux ratio is changing across the circum-nuclear region (an example is shown in Fig. 3). It indicates (as well as the dimension of the continuum source, see Fig. 2) that the contribution to the continuum is coming not only from the nucleus, but also from the circum-nuclear region. The blue bump (see Fig. 3) in the continuum flux may be caused by the UV-radiation from an accretion disk or by the violent star-formation in the circum-nuclear ring. Note that a similar effect can be caused by the different dust absorption (inartistic reddening) across the central part.

3.2. Fe II emission region in Mrk 493

As it can be seen in Table 1, 3D spectra of Mrk 493 were observed in two epochs, in 2004 and 2007. Consequently, first we were looking for the line/continuum changes between these epochs. To do that, we found a summary spectra for both epochs around the central part. To avoid errors caused by procedure of spectra elaboration (flux calibration, different number of spaxels taken in summary spectra in different epochs, etc.) we normalized both spectra on the maximal intensity of the $H\beta$ line. In Fig. 4, we presented the normalized spectra to the maximal intensity of the $H\beta$ line. As it can be seen in Fig. 4, there is no significant difference between the spectra (in the lines and continuum) observed in these two epochs (a three-year period). Only, a slight difference can be noted in the $\text{He II}\lambda 4686\text{\AA}$ wavelength range (see Fig. 4, down), that is probably caused by changing in this line. A marginal difference between the spectra (see Fig. 4 down, for $\lambda < 4750\text{\AA}$) is caused by different spectral resolution (see Table 1). Note here that Klimek et al. (2004) found a slight long-term variation in V-band of Mrk 493 ($\sim \pm 0.15^m$, see their Fig. 18).

In order to find the parameters of the Fe II line emitting region and its possible correlation with the $H\beta$ line emitting one, we use the high resolution spectra. We fitted the Fe II and $H\beta$ lines in the nucleus region in order to compare the kinematic parameters of the Fe II and $H\beta$ line emitting regions (Fig. 5). Also, we fitted the $H\alpha + [\text{NII}]$ wavelength band (Fig. 6) in the low-resolution spectral data cube in order to compare kinematics of the $H\beta$ and $H\alpha$ emitting regions.

There are several ways to fit Fe II template (red and blue shelf, see e.g. Boroson & Green 1992, Popović et al. 2004, Veron et al. 2006, etc.). We use a template of 53 the most intensive Fe II lines in the spectral interval from 4400 \AA to 5400 \AA from five types of transitions with $3d^6(^3F_2)4s^4F$, $3d^54s^2^6S$, $3d^6(^3G)4s^4G$, $3p^63d^7^2D$ and $3d^6(^5D)4s^6D$ lower level configurations. Each of the 53 lines is assumed to have Gaussian profile.

To constrain the number of fitting parameters, we assumed:

(i) all Fe II lines are coming from the same emitting region, therefore the widths (W) and shifts (d) of the Gaussians representing the lines are the same;

(ii) the line intensities within one transition defined by low level configuration have been connected with the relation (Kovačević et al. 2008):

$$\frac{I_1}{I_2} \approx \left(\frac{\lambda_2}{\lambda_1}\right)^3 \frac{f_1}{f_2} \cdot \frac{g_1}{g_2} \quad (1)$$

where I_1 and I_2 are intensities of the lines with the same lower level of a transition, λ_1 and λ_2 are line transition wavelengths, g_1 and g_2 are corresponding statistical weights, and f_1 and f_2 the oscillator strengths, E_1 and E_2 are energies of the upper level of transitions.

(iii) the intensity ratio of the [OIII] $\lambda\lambda$ 4959,5007 Å lines was fixed as 1:3 (see Dimitrijević et al. 2007), and we also assumed that all narrow lines ([OIII] and narrow H β) have the same width and shift.

(iv) In summary, we fitted the wavelength region FeII+H β + [OIII] with a sum of Gaussian functions (Fig. 5A), from which 53 represents the Fe II template (having the same widths and shifts, Fig. 5C). To find the best fit we use χ^2 minimization routine.

Also, we used low resolution spectra to fit (with the same sum of Gaussian functions) the H α and H β lines. We were able to find a good and consistent fit (having the similar parameters for corresponding Gaussian function in both lines) using three-Gaussian fitting (see Figs. 5 and 6). Two Gaussian model for broad H α and H β cannot properly fit the lines profiles, since there are far wings in these lines (especially in H α , see Fig. 6). Moreover, a F-test shows that the three Gaussian assumption is statistically better than the two Gaussian one. Note here that often three regions in AGN have been considered (see e.g. Sulentic et al. 2000). Consequently, we fitted H α and H β with three Gaussian functions, aiming that the parameters of Gaussian for the same spectrum (obtained from

one spaxel) have similar values for both lines (fitting the spectra observed in 2007). Note here that recently Hu et al. (2008a) reported that the BLR of AGN is composed from two emitting regions.

We were able to fit the emission lines from 16 and 21 spaxels of high (observed in 2004) and low (observed in 2007) resolution spectra, respectively. In both cases, we selected only spectra around the center where in each of them the $H\beta$ or/and $H\alpha$ can be decomposed into three components (broad - W_B , intermediate W_I and narrow W_{NLR}) and where the signal-to-noise ratio was enough good that the far wings are well defined. The parameters of the best fit of spectra from each spaxel are given in Tables 2-4. In Table 2-3 the parameters of the best fit for 16 high resolution spectra are presented. As it can be seen from Tables 2-3, the obtained parameter values for different spaxels are consistent, and differences between a parameter from different spaxels is probably caused by the accuracy of the fitting procedure. The same is in the case of the low resolution spectra (Table 4). As one can see from Tables 2-3, the averaged values of widths of the $H\beta$ line components are: $W_B=(2380\pm 200)$ km/s, $W_I=(790\pm 80)$ km/s and $W_{NLR}=(250\pm 40)$ km/s² (W_{NLR} is assumed to be the same as the narrow [OIII] line width). The broadest component is weak and it is interesting that it is slightly more intensive than the $He\lambda 4686$ line (Gaussian represented with solid line left from the $H\beta$ in Fig. 5B). In all spectra the broadest component shows the blue shift of $-(429\pm 133)$ km/s with respect to the narrow [OIII] lines, while the intermediate component shows a slight redshift; in average $+(156\pm 47)$ km/s, that is in the frame of fitting errors. Also, there is no significant difference between the Gaussian parameters across the nucleus part, the difference is probably caused by accuracy of the fitting with three Gaussian functions. It means that we were not able to find significant differences in

² W is taken from Gaussian function $exp(-(\delta\lambda - d/W)^2)$ and it is connected with velocity dispersion (σ) and Full Width at Half Maximum (FWHM) as $W = \sqrt{2}\sigma = FWHM/2\sqrt{\ln(2)}$

gas kinematics across the nuclear part.

Also, we fitted the $H\beta$ and $H\alpha$ lines from the low resolution spectra (observed in 2007, 21 spaxels). The parameters of the best fit for $H\alpha$ are given in Table 4. The obtained parameters for $H\beta$ from this spectra are similar to the parameters shown in Tables 2 and 3 (for high resolution spectra), but showing systematically slight larger widths caused by lower resolution. As one can see from Table 4, the $H\alpha$ ($W_{BLR} \sim 1800$ km/s and $W_{ILR} \sim 650$ km/s) has a smaller width and shift than $H\beta$. The difference in the shift and width between the broad and intermediate $H\alpha$ and $H\beta$ may be caused partly by fitting procedure and partly by different spectral resolution.

The Fe II line widths from different spaxels indicate the velocity gas in the Fe II emission region around $W_{FeII} \approx 800$ km/s (an averaged value 760 ± 50 km/s, see Table 2), that corresponds to the random velocity in the intermediate region (as well as the shift, see Tables 2 - 4). This fact suggests that the Fe II line could be originated in an intermediate line region as it was mentioned in Popović et al. (2004). Moreover, recently Kuehn et al. (2008) suggested that the optical Fe II emission of Ark 120 does not come from a photoionization-powered region similar in size to the $H\beta$ (broad component) emitting region, i.e. they conclude that Fe II emission come from a photoionized region several times larger than the $H\beta$ one, or from gas heated by some other mechanism (not by photoionization). Moreover, Hu et al. (2008b) found the the line width of Fe II is significantly narrower than that of the broad component of $H\beta$ in a sample of 4037 AGN. All of the results mentioned above as well as our fitting results for the Fe II lines suggest that a large fraction of the Fe II emission arise in the outer parts of the BLR, i.e. Fe II emission may be originated in the intermediate-line region, which may be the transition from the torus to the BLR (or an accretion disk, see e.g. Popović et al. 2004). From this observations is hard to say if the portion of the Fe II emission is formed in the BLR, since the BLR component is too weak

even in the Balmer lines (Figs. 5 and 6) and contributes around 25-40% to the total line flux of Balmer lines (see Tables 3 and 4). The Fe II emission is strong and the flux ratio of the Fe II emission (integrated in the interval 4400 Å to 5500 Å) and H β -total line flux is 0.52 ± 0.08 .

The Fe II emission spectra formation from AGN is still poorly understood (Joly 1993; Hamann & Ferland 1999, Collin & Joly 2000). Typically, photoionization cloud models for the BLR fail to account for the observed strength of the Fe II emission. The mechanism that is responsible for Fe II origin is supposed to be the collisional excitation (see e.g. Sigut & Pradhan 2003), i.e. inelastic collisions with electrons excite the odd parity levels near 5 eV which then decay into the optical and UV lines. This mechanism is efficient whenever the gas temperature is above 7000 K, temperatures which are generally found in photoionized models of the BLR. Excitation is irrespective of the local optical depth in the Fe II lines, and thus this mechanism does not suffer limitations of the continuum fluorescence. It is generally believed that collisional excitation is responsible for the bulk of the Fe II emission. Also, Collin & Joly (2000) proposed that Fe II emission can be explained by a non-radiative heating mechanism, as e.g. shocks, with an overabundance of iron. Comparison of AGN with other objects emitting strong Fe II lines is in favor of the presence of strong outflows and shocks. It is interesting here that we could not register significant outflow in the Fe II emitting region of Mrk 493, but there is a systematic blueshift of the broad H α and H β component. This asymmetry can indicate some kind of the outflow. Note here that Hu et al. (2008b) found that majority of quasars (from a sample of 4037 quasars) show redshifted Fe II emission toward to red around 400 km/s.

3.3. The source of ionization of the NLR of Mrk 493

In order to identify the nature of the gas ionization source in Mrk 493, we constructed diagnostic diagrams using the narrow emission-line intensity ratios. In Fig. 8 we present $[\text{O III}]/\text{H}\beta$ vs. $[\text{N II}]/\text{H}\alpha$ and $[\text{O III}]/\text{H}\beta$ vs. $[\text{S II}]/\text{H}\alpha$. According to Veilleux & Osterbrock (1987) we separated the regions corresponding to the ionization by AGN, young OB-stars (H II regions) and shock waves (LINERS) on the diagrams.

It was surprising, that all points are only in the H II region, implying that the main source of ionization should be young hot stars from violent star formation in the center of Mrk 493.

From these diagrams we can conclude that the low ionization lines are primarily excited by star formation. No any contribution to line ionization from AGN continuum is seen in Fig. 8.

In the analysis is not taken into account a possible absorption in the $\text{H}\alpha$ and $\text{H}\beta$ lines. In any case the stellar absorption reduction would increase of the $\text{H}\alpha$ and $\text{H}\beta$ fluxes, consequently the $[\text{OIII}]/\text{H}\beta$ ratio would be lower; and points presented in Fig. 7 would be deeper in the H II section of the graph. Therefore, we can point out that star forming process is probably a dominant source of ionization in the central part of Mrk 493.

3.4. The circum-nuclear ring

As it can be seen in Fig. 1, in the central part of the Mrk 493, a circum-nuclear ring of star-formation is present, already mentioned by Deo et al. (2006), see also new HST/ACS observations in the UV domain (Muñoz-Marín et al. 2007). As it can be seen in Fig. 1, this is a prototypical galaxy with a strong large-scale bar with leading edge dust lanes feeding a central nuclear ring and a grand-design spiral toward the center. From the HST

images, it can be seen a presence of multiple dust spiral arms outside the nuclear ring. Note here that the radius of the ring (0.6-0.8 arcsec corresponding 350-500 pc) is under the spatial resolution of our MPFS data, but there is also an extensive continuum emission (elliptical shape, see Fig. 2) that is probably coming from emission gas around this ring.

All properties of the ring (its size, location inside the strong bar, morphology of dust lanes) indicate the resonance origin of this structure. It seems to be a nuclear ring formed near the Inner Lindblad Resonance (ILRe) of a large-scale bar (see Buta & Combes, 1996 for details). According to the common point of view a large-scale bar efficiently drives gas from the outer disk into the inner region where the gas flow stops near the ILRe where the powerful starburst are commonly observed (for instance, see review by Jogee 2006).

We roughly estimated the total rate of starformation in the circum-nuclear region using the formula from Kennicutt (1998) which connects the SFR with the $H\alpha$ luminosity ($L_{H\alpha}$). From MPFS data we estimated the $L_{H\alpha} = 6.7 \times 10^{41} \text{ erg s}^{-1}$ in the aperture radius of 2.5 arcsec. This luminosity corresponds to $\text{SFR}=5M_{\odot}/\text{yr}$. Of course, the total $L_{H\alpha}$ includes also the nuclear AGN contribution and therefore the SFR value is overestimated. In Table 4, we give the estimated contribution of the broad $H\alpha$ component (and intermediate one) to the total flux of $H\alpha$ (columns 7 and 8) and as it can be seen from Table 4, around 40% of $H\alpha$ is emitted in the narrow $H\alpha$ line. Consequently, it can indicate the $\text{SFR}=2M_{\odot}/\text{yr}$, that is unusually large for such compact region (less than one kiloparsec in the diameter).

In a such system it is interesting to see the spectra further from the centra. Even we have very weak spectra outside $3'' \times 3''$, we were able to see the weak $H\alpha$ and $H\beta$ lines in the spaxels located at $4''$ from the center (Fig. 8, upper panel). In Fig. 8 (upper panel) we showed the spectrum extracted from three spaxels: at the center ((0,0) - top), $2''$ far from the center ((0,2) - middle) and $4''$ far from the center ((0,4) - down). To compare these three spectrum, the last two spectra are magnified by 3 and 27 times, respectively.

Although the spectra at (0,4) is very noisy we were able to compare the $H\alpha$ line profile from this spectrum (solid line in Fig. 8, panel bottom) with the two closer to the center (dashed and dashed-dotted line for spectra from 0" and 2", respectively – see Fig. 8 panel down). Also, we normalized the $H\alpha$ lines to one. As it can be seen from Fig. 8, the line profiles of $H\alpha$ from 0" and 2" are almost identical, while $H\alpha$ from (0,4) tends to have stronger [NII] emission, but it should be taken with caution since small signal-to-noise ratio in this spectrum. It is interesting that the $H\alpha$ line profiles are similar, i.e. that broad wings are present in the $H\alpha$ line at 4" from the center. It may also indicate that some other mechanism can contribute to the origin of the broad Balmer line component in Mrk 493 (non-AGN component)

Since the stellar ring is located in the central part of the line emission regions one can speculate that the ring may be in principle star forming region. It is interesting that the radiation of young stars from the ring probably represents the source of ionization of the line emitting regions in Mrk 493. Moreover, the strong Fe II emission and weak [OIII] one, can be explained with a model that contains massive starburst (SB) plus an AGN (see e.g. L ipari & Terlevich 2006, etc.). The SB+AGN can lead to large scale expanding supergiant shells (see e.g. L ipari et al. 1994, Lawrence et al. 1997, Canalizo et al. 1998, L ipari & Terlevich 2006). In the case of Mrk 493, it might be that the Fe II lines are also formed in the gas located in (or around) the ring. The question is why the Fe II lines are broad around 800 km/s? Note here that bloated stars extended envelopes are similar, in many ways, to the low density gas. Close to the center they will show typical BLR spectrum and further away a typical NLR spectrum (Netzer 2006). Since violent star formation processes are in the central part of Mrk 493, and our analysis of ionizing diagrams shows that the ionization source is only thermal, we can not exclude a possibility that the star formation process is the main mechanism of radiation in the center of this galaxy. Moreover, the active star formation-regions have been found in Seyfert galaxies (see e.g. Davies et al. 2004, 2007;

Muñoz-Maríne et al. 2007, and references therein). E.g. Davies et al. (2007) found that in the case of nine Seyfert galaxies, on kpc scale, the stellar luminosity is comparable with AGN one.

4. Conclusion

In this paper we report the 3D spectrophotometric observations of the Mrk 493. From our investigation we can give the following conclusions:

(i) The continuum and [SII] line emitting regions in Mrk 493 seem to be very extensive ([SII] up to 1 kpc, and continuum $>1\text{kpc}$), and they are larger than the [OIII], Fe II and Balmer emission line regions.

(ii) It seems that the strong Fe II emission is not coming from the BLR ($W_{BLR} \sim 2000$ km/s), but from a region with velocity dispersion around 800 km/s. This is in an agreement with some earlier investigation given by Popović et al. (2004) and recent ones given by Kuehn et al. (2008) and Hu et al. (2008) that a large fraction of the Fe II emission may come from an ILR.

(iii) There is no changes of the continuum and emission lines (instead He II λ 4686) between two observations (in the three-year period), that may also indicate non-BLR origin of lines. Otherwise, the BLR in Mrk 493 should be a): very extensive $\sim 1\text{pc}$ and/or b) very stable.

(iv) The source of ionization of the narrow Balmer and [OIII] line emitting regions in Mrk 493 seems to not be the nucleus, but the star-forming processes;

(v) The position of the line and continuum regions coincides with a composite nuclear region: an AGN plus a circum-nuclear star-forming ring observed in the HST UV/optical

images, but it seems that the emitting source of the narrow line and continuum is probably the circum-nuclear star-forming ring, but here remains a question about the mechanism of the Fe II production in a such ring.

Acknowledgments

This work is based on the observational data obtained with the 6-m telescope of the Special Astrophysical Observatory of the Russian Academy of Sciences funded by the Ministry of Science of the Russian Federation (registration number 01-43) and from the data archive of the NASA/ESA Hubble Space Telescope at the Space Telescope Science Institute. This work was supported by the Ministry of Science of Serbia through the project (14002) ”Astrophysical Spectroscopy of Extragalactic Objects”. Also, the work has been financed by the Russian Foundation for Basic Research (project no. 06-02-16825). A.V.M. acknowledges a grant from the President of the Russian Federation. We would like to thank to the referee for very useful comments.

REFERENCES

- Afanasiev, V. L., Dodonov, S. N., Moiseev, A. V., 2001, in Ossipkov L. L., Nikiforov I. I., eds, Proc. Int. Conf. Stellar Dynamics: from Classic to Modern, Sobolev Astron. Inst. St Petersburg, p. 103
- Afanasiev, V.L., Moiseev, A.V., 2005, *Astronomy Letters*, 31, 194 [astro-ph/0502095]
- Arribas, S., Mediavilla, E., García-Lorenzo B., del Burgo C., and Fuensalida J.J., 1999, *A&AS*, 136, 189
- Boller, T., Brandt, W. N., Fink, H. 1996, *A&A*, 305, 53
- Boroson, T. A., Green, R. F. 1992, *ApJS*, 80, 109
- Botte, V., Ciroi, S., Rafanelli, P., Di Mille, F. 2004, *AJ*, 127, 3168
- Buta, R., Combes, F., 1996, *Fundam. Cosm. Phys.*, 17, 95
- Canalizo, G., Stockton, A., Roth, K. 1998, *AJ*, 115, 890
- Collin, S., Joly, M. 2000, *NewA Rev.*, 44, 531
- Crenshaw, D. M., Peterson, B. M., Korista, K. T., Wagner, R. M., Aufdenberg, J. P. 1991, *AJ*, 101, 1202
- Davies, R.I., Tacconi, L.J., Genzel, R. 2004, *ApJ*, 613, 781
- Davis, R.I., Mueller Sánchez, F., Genzel, R., Tacconi, L.J., Hicks, E.K.S., Friedrich, S. 2007, *ApJ*, 671, 1388.
- Deo, R.P., Crenshaw, D.M., Kraemer, S.B, 2006, *AJ*, 132, 321
- Dimitrijević, M. S., Popović, L. Č., Kovacević, J., Dačić, M., Ilić, D. 2007, *MNRAS*, 374, 1181

- Glozzi, M., Papadakis, I. E., Brinkmann, W. P. 2007, ApJ, 656,
- Hamann, F., Ferland, G. 1999, ARA&A, 37, 487
- Hu, C., Wang, J. M., Chen, Y. M., Bian W. H., Xue S. J., 2008, ApJL, 683, 115
- Hu, C. Wang, J.-M. Ho, L. C., Chen, Y.-M., Zhang, H.-T., Bian, W.-H., Xue, S.-J. 2008, ApJ, 687, 78
- Joly, M. 1993, Ann. Phys. Fr., 18, 241
- Jogee, S., 2006, Lecture Notes in Physics, 693, 143
- Kennicutt, R.C., 1998, ARA&A, 36, 189
- Klimek, E.S., Gaskell, M. C., Hedrick, C. H. 2004, ApJ, 609, 69.
- Komossa, S. 2008, Rev. Mex. AA C, 32, 86
- Kovačević, J., Popović, L. Č., Dimitrijević, M. S. 2008, in preparation.
- Kuehn, C. A., Baldwin, J. A., Peterson, B. M., Korista, K. T. 2008, ApJ, 673, 69
- Lawrence, A., Elvis, M., Wilkes, B., McHardy, L., Brandt, N. 1997, MNRAS, 285, 879
- Leighly, K. M. 1999a, ApJS, 125, 317
- Leighly, K. M. 1999b, ApJS, 125, 297
- Lípari, S.L., Terlevich, R.J. 2006, MNRAS, 368, 1001.
- Lipari, S., Colina, L., Macchetto, F. 1994, ApJ, 427, 174
- Moiseev A.V., Valdés J.R., Chavushyan V.H., 2004, A&A, 421, 433
- Mathur, S. 2000 NewAR, 44, 469

- Muñoz-Marín V.M., González Delgado R.M., Schmitt H.R., Cid Fernandes R., et al., 2007, *AJ*, 134, 648
- Nagao, T., Murayama, T., Taniguchi, Y. 2001, *ApJ*, 546, 744
- Netzer, H. 2006, in ‘Physics of Active Galactic Nuclei at all Scales’, eds. by Alloin D., Johnson R. and Lira P., *Lecture Notes in Physics*, 693, 1
- Osterbrock, D. E., Pogge, R. W. 1985, *ApJ*, 297, 166
- Popović, L. Č., Mediavilla, E., Bon, E., Ilić, D. 2004, *A&A*, 423, 909.
- Sigut, T.A.A. & Pradhan, A.K. 2003, *ApJS*, 145, 15
- Sulentic, J. W., Marziani, P., & Dultzin-Hacyan, D. 2000, *ARA&A*, 38, 521
- Wang, J.-M., Zhang, E.-P. 2007, *ApJ*, 660, 1072
- Veilleux, S., Osterbrock, D. M., 1987, *ApJS*, 63, 295
- Veron-Cetty, M.-P., Joly, M., Veron, P., Boroson, T., Lipari, S., Ogle, P. 2006, *A&A*, 451, 851

Table 1: Log of MPFS observations.

Date	T_{exp} (sec)	Sp. Range (\AA)	Sp. Res. (\AA)	Seeing (arcsec)
2004 May 21	4800	4150 - 5650	4	1.5 ± 0.2
2007 May 18	7200	4300 - 7200	8	1.7 ± 0.2

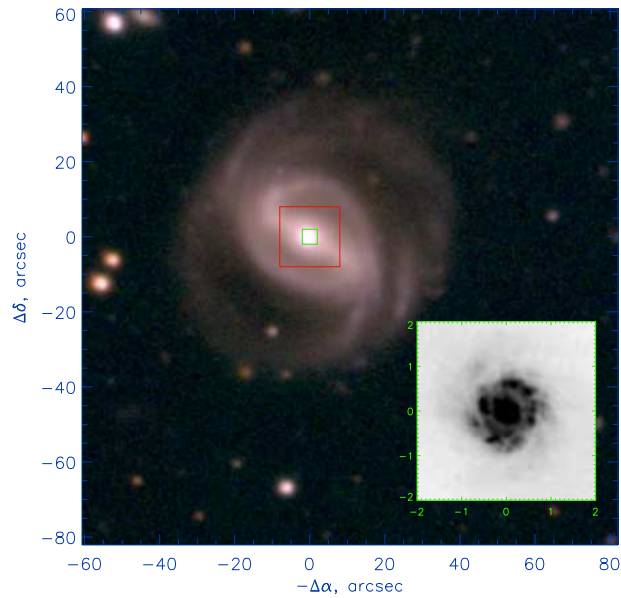


Fig. 1.— The composite BVR_C color image obtained with SCORPIO at 6-m telescope. The large red box shows the region observed with MPFS. The small green box marks the field shown in the bottom right corner. It is the HST WFPC2 image in the optical band with F606W filter.

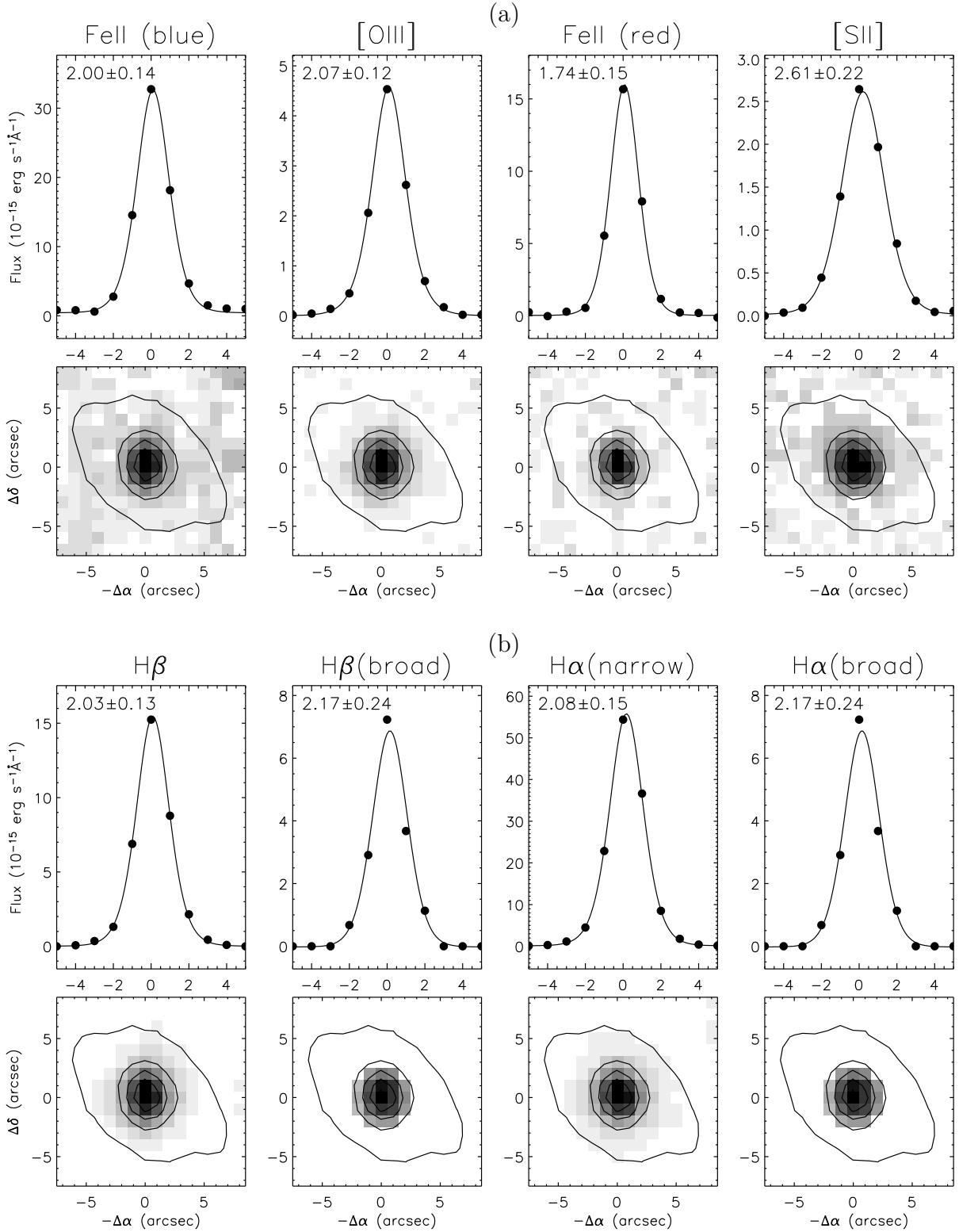


Fig. 2.— The circum-nuclear region of Mrk 493 observed with MPFS. The maps in the [OIII] $\lambda 5007$, [SII] $\lambda 6717, 6731$ and Fe II lines (a) and in narrow and broad components of the Balmer lines (b). The contours represent the continuum measured near $\lambda 6200 \text{Å}$. Top row shows the cross-sections of the nuclear emission along the horizontal axis. The points

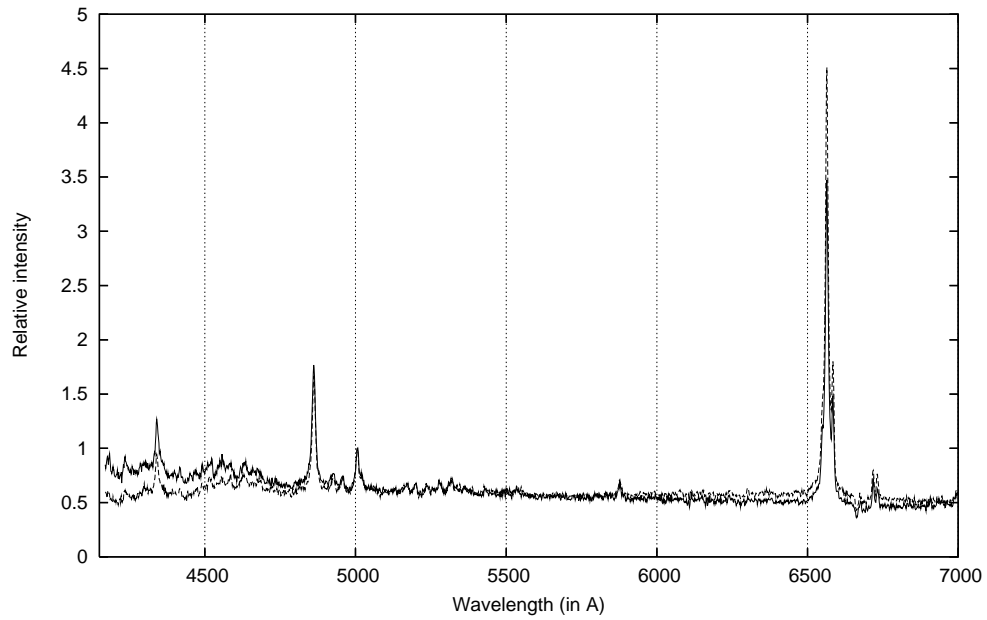


Fig. 3.— Comparison of spectra from different spaxels, with coordinates relative the nucleus ($\Delta\alpha = -1''$, $\Delta\delta = -2''$) and ($\Delta\alpha = +2''$, $\Delta\delta = +1''$), of Mrk 493. The spectra are normalized to the maximum of the $H\beta$ line.

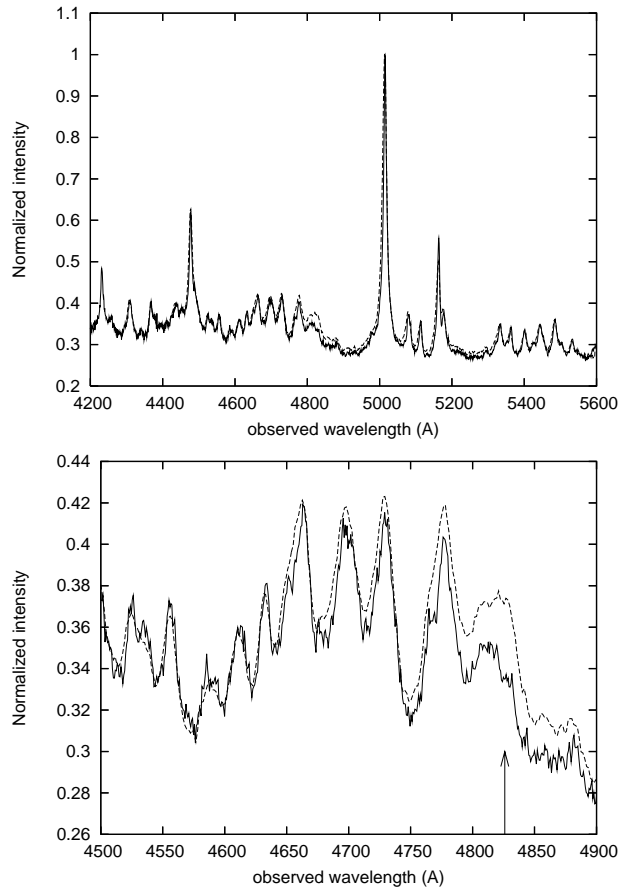


Fig. 4.— Panel up: The Mrk 493 spectra in the $H\beta$ +Fe II wavelength band normalized to the maximum of the $H\beta$ intensity, observed in 2004 (solid line) and 2006 (dashed line). Panel down: The blue Fe II template observed in 2004 (solid line) and 2006 (dashed line), the arrow shows the position of the He II λ 4686 line in observed wavelength scale.

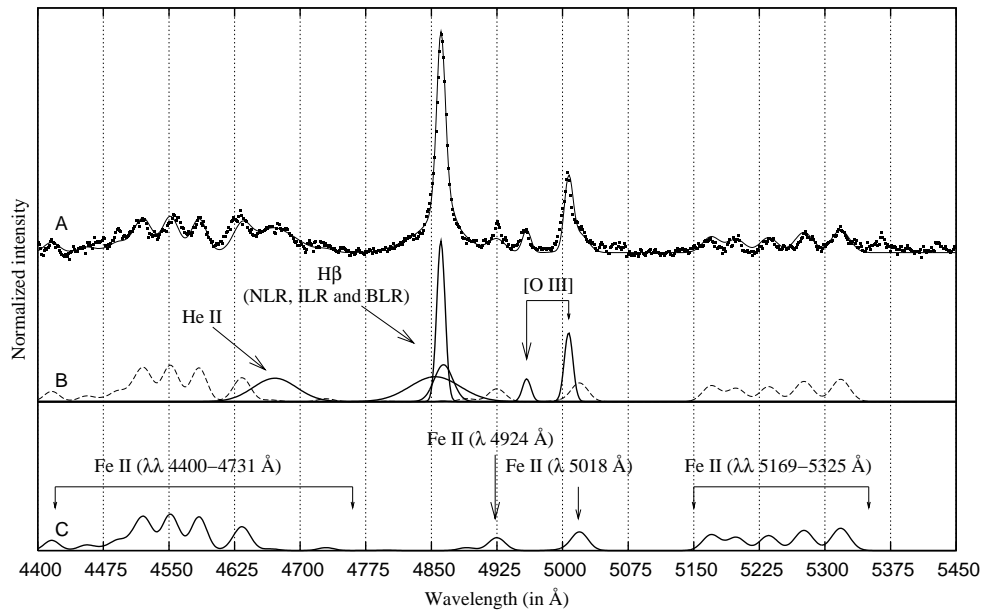


Fig. 5.— The decomposition of the observed H β spectral region (dots) using the χ^2 best fit minimization (C). The Gaussian functions denoted with solid lines in panel B represent the components of He II, H β and [OIII]. The Fe II template obtained from the best fit (53 Gaussian functions) is presented in panel C.

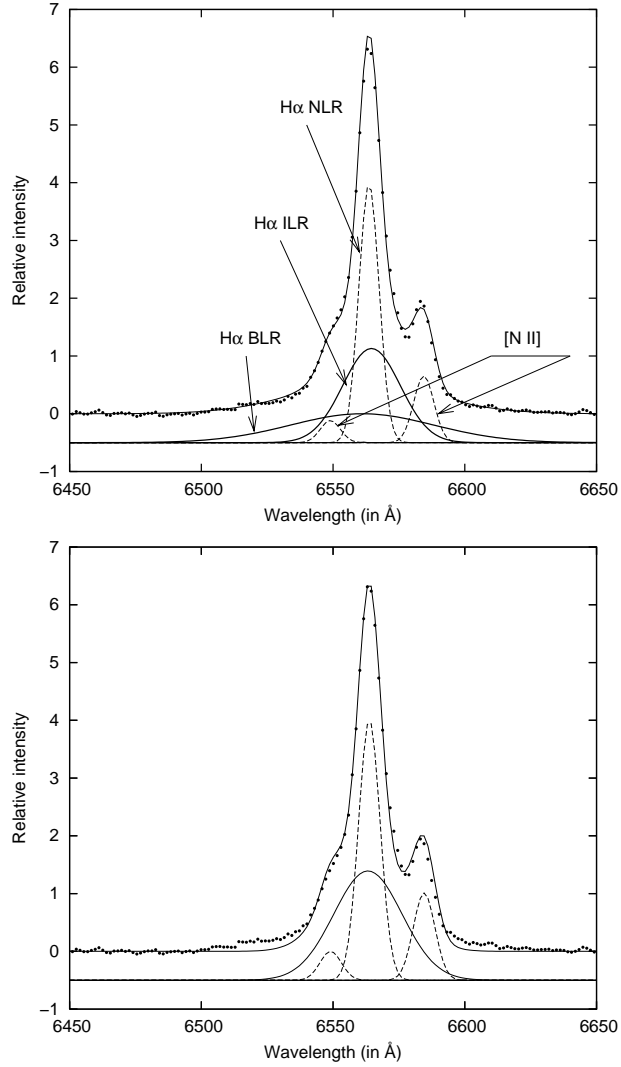


Fig. 6.— The decomposition of the observed $H\alpha+[NII]$ spectral lines (dots) where $H\alpha$ is decomposed with three (up) and two (down) Gaussian functions.

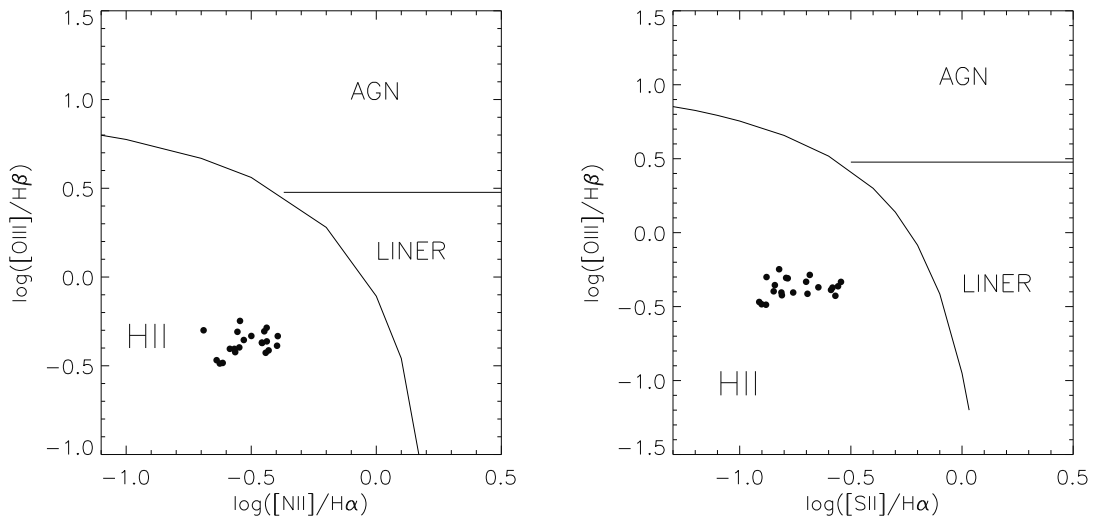


Fig. 7.— The diagnostic diagrams of Mrk 493 nucleus. Only narrow Balmer line component is included. A dot presents the line flux ratio obtained from the same spaxel.

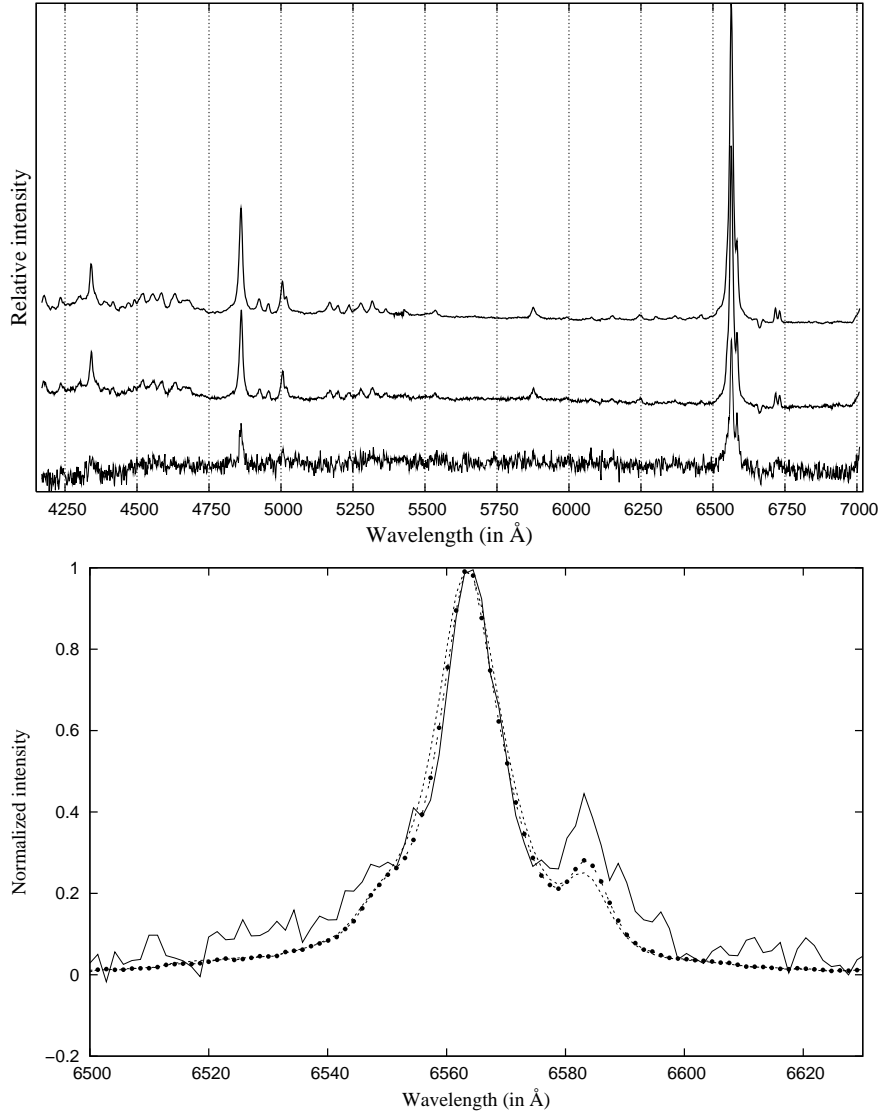


Fig. 8.— *Top:* The spectrum from central spaxel (0,0) - up, from 2'' from the center, (0,2) spaxel -middle and from 4'' from the center, (0,4) spaxel -down. The spectrum from spaxel (0,2) was multiplied with factor 3 and spectrum from spaxel (0,4) with factor 27. *Down:* The H α lines are normalized to one from these three spectra: central spaxel (0,0) – dashed line, spaxel (0,2) – dashed-dotted line, and spaxel (0,4) – solid line.

Table 2: The parameters of the best fit for the [O III] $\lambda\lambda 4959, 5007 \text{ \AA}$ lines and Fe II template ($\lambda\lambda 4400\text{-}5400 \text{ \AA}$) for each spaxel (16 spectra from 2004 observations). Used notation: 'position' - the position of the spaxel in arc seconds, where (0,0) is the central part; w [O III] - width of the [OIII]; [O III]/H β - the flux ratio of the [O III] and H β total flux; w Fe II and sh Fe II - widths and shifts of Fe II lines, respectively; Fe II $_{total}$ /H β - the flux ratio of the Fe II $_{total}$ and H β (total flux)

position	w [O III]	[O III]/H β	w Fe II	sh Fe II	Fe II $_{total}$ /H β
(0, 0)	310	0.058	780	79	0.56
(+1, 0)	290	0.057	720	83	0.48
(- 1, 0)	280	0.061	840	24	0.69
(0, +1)	270	0.045	770	48	0.48
(0, -1)	270	0.051	840	50	0.60
(+1, -1)	260	0.055	870	18	0.59
(+1, +1)	270	0.060	810	67	0.49
(- 1, +1)	250	0.054	720	80	0.48
(- 1, -1)	250	0.048	720	48	0.59
(0, -2)	290	0.069	720	40	0.61
(+1, -2)	260	0.061	720	78	0.46
(- 1, -2)	190	0.045	720	23	0.48
(0, +2)	230	0.058	720	50	0.40
(+1, +2)	240	0.071	720	96	0.49
(+2, 0)	200	0.059	750	-52	0.46
(+2, -1)	170	0.051	750	-67	0.47
average val.	250 \pm 40	0.056 \pm 0.007	760 \pm 50	42 \pm 46	0.52 \pm 0.08

Table 3: The same as in Table 2, but for the $H\beta$ BLR, ILR and NLR components. The width and shift of the $H\beta$ NLR component is assumed to be the same as one of the [OIII] lines.

position	w BLR $H\beta$	w ILR $H\beta$	sh BLR $H\beta$	sh ILR $H\beta$	$H\beta$ BLR/ $H\beta$	$H\beta$ ILR/ $H\beta$	$H\beta$ NLR/ $H\beta$
(0, 0)	2490	840	-267	205	0.35	0.35	0.30
(+1, 0)	2490	820	-633	191	0.33	0.40	0.27
(- 1, 0)	2490	900	-294	100	0.31	0.34	0.35
(0, +1)	2820	810	-647	184	0.38	0.35	0.27
(0, -1)	2440	670	-631	171	0.34	0.44	0.22
(+1, -1)	2480	860	-277	172	0.31	0.36	0.33
(+1, +1)	2490	940	-170	176	0.30	0.39	0.32
(- 1, +1)	2400	800	-443	95	0.43	0.29	0.29
(- 1, -1)	2400	800	-434	209	0.38	0.25	0.37
(0, -2)	2400	840	-423	115	0.40	0.29	0.30
(+1, -2)	2400	810	-410	188	0.43	0.26	0.30
(- 1, -2)	2100	690	-424	114	0.50	0.27	0.22
(0, +2)	2400	800	-432	105	0.48	0.32	0.21
(+1, +2)	2100	750	-397	141	0.37	0.38	0.25
(+2, 0)	2100	670	-418	242	0.40	0.22	0.38
(+2, -1)	2100	690	-444	93	0.49	0.23	0.28
average val.	2380±200	790±80	-421±133	156±47	0.39±0.06	0.32±0.06	0.29±0.05

Table 4: The same as in Table 2, but for 21 spectra (observed in 2007) of the H α BLR, ILR and NLR components.

position	w BLR H α	w ILR H α	w NLR H α	sh BLR H α	sh ILR H α	$\frac{H\alpha_{BLR}}{H\alpha}$	$\frac{H\alpha_{ILR}}{H\alpha}$	$\frac{H\alpha_{NLR}}{H\alpha}$
(0, 0)	2460	700	300	-196	-16	0.24	0.35	0.41
(+1, 0)	1980	750	300	-352	13	0.18	0.42	0.39
(- 1, 0)	1980	750	300	-359	14	0.23	0.32	0.45
(0, +1)	1980	690	300	-265	4	0.22	0.37	0.41
(0, -1)	1740	640	310	-216	9	0.24	0.34	0.42
(- 1, +1)	2040	700	290	-184	5	0.25	0.32	0.43
(+1, +1)	2040	650	280	-169	13	0.27	0.36	0.37
(- 1, -1)	2040	680	270	-181	14	0.26	0.33	0.42
(+1, -1)	2040	640	280	-139	10	0.26	0.34	0.40
(- 1, +2)	2040	820	300	-143	-90	0.22	0.23	0.55
(0, +2)	1770	700	290	-129	-15	0.23	0.29	0.48
(+1, +2)	1770	650	270	-121	22	0.30	0.28	0.42
(- 2, +1)	1770	560	300	-135	-24	0.23	0.24	0.54
(+2, +1)	1770	640	250	-139	25	0.29	0.34	0.37
(- 2, 0)	1560	580	250	-142	16	0.29	0.36	0.35
(+2, 0)	1560	580	230	-138	26	0.25	0.42	0.33
(- 2, -1)	1560	630	250	-128	33	0.27	0.34	0.39
(+2, -1)	1560	600	260	-136	24	0.33	0.28	0.40
(- 1, -2)	1530	610	220	-139	51	0.29	0.37	0.35
(0, -2)	1530	570	250	-137	46	0.29	0.34	0.37
(+1, -2)	1530	560	230	-126	31	0.31	0.40	0.29
av. val.	1820 \pm 250	650 \pm 70	270 \pm 30	-175 \pm 70	10 \pm 30	0.26 \pm 0.03	0.33 \pm 0.05	0.41 \pm 0.06